



# Hydrogen trapping and embrittlement of titanium- and vanadium carbide-containing steels after high-temperature hydrogen charging

Tim Boot<sup>1,\*</sup> , Athira Suresh Kumar<sup>2,3</sup> , Santhana Eswara<sup>2</sup> , Pascal Kömmelt<sup>4</sup>, Amarante Böttger<sup>1</sup> , and Vera Popovich<sup>1</sup>

<sup>1</sup> Department of Materials Science and Engineering (MSE), Mechanical Engineering (ME), Delft University of Technology, Mekelweg 2, 2628 CD Delft, The Netherlands

<sup>2</sup> Materials Research and Technology Department, Advanced Instrumentation for Nano-Analytics (AINA), Luxembourg Institute of Science and Technology, 41 Rue du Brill, 4422 Belvaux, Luxembourg

<sup>3</sup> University of Luxembourg, 2 Avenue de l'Université, 4365 Belvaux, Luxembourg

<sup>4</sup> Research and Development, TATA Steel, PO Box 10000, 1970 CA IJmuiden, The Netherlands

**Received:** 16 November 2023

**Accepted:** 23 March 2024

**Published online:**  
25 April 2024

© The Author(s), 2024

## ABSTRACT

This work studies the effect of TiC and VC precipitate sizes on hydrogen trapping and embrittlement. Two experimental ferritic HSLA steels containing either TiC or VC carbides for precipitation strengthening are annealed in nitrogen and hydrogen gas. This results in a hydrogen uptake of up to 0.91 and 0.44 wppm in the TiC and VC steels, respectively. TEM and TDS analysis indicate that semi-coherent TiC particles trap hydrogen in misfit dislocations with an activation energy of 43 kJ/mol. Coherent VC particles are suggested to trap hydrogen in interface carbon vacancies, with an energy between 53 and 72 kJ/mol. Carbon vacancies are the likely trapping site in incoherent precipitates, where SIMS imaging confirms that incoherent TiC precipitates trap preferentially near the interface, whereas incoherent VC precipitates trap throughout their bulk. Neither alloy is embrittled in SSRT tests after hydrogen absorption, which shows that these precipitates can be used as both a hydrogen sink and a strengthening mechanism in steels.

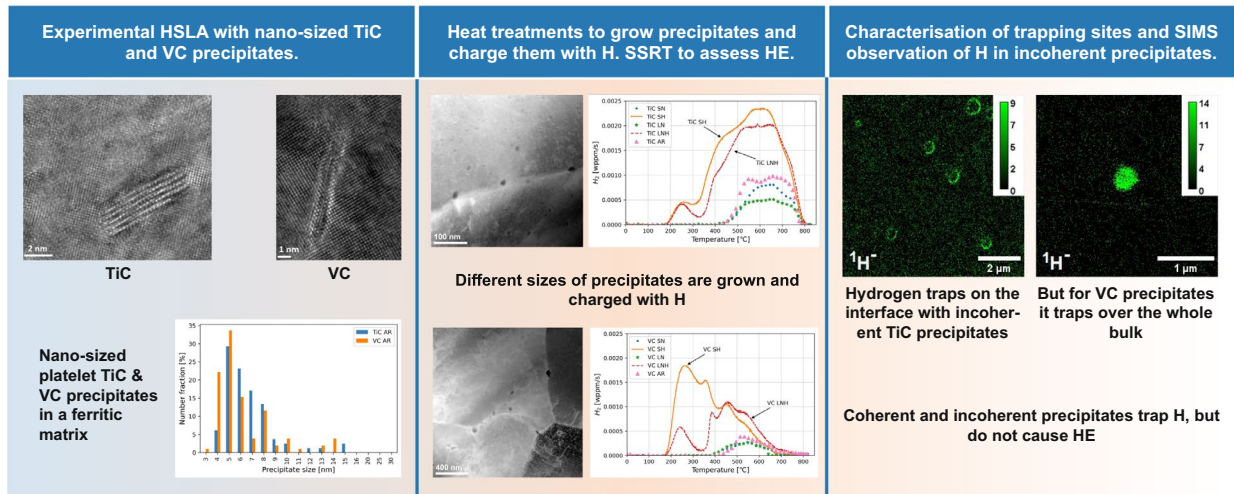
Handling Editor: P. Nash.

Athira Suresh Kumar, Santhana Eswara, Pascal Kömmelt, Amarante Böttger, and Vera Popovich have contributed equally to this work.

Address correspondence to E-mail: t.boot@tudelft.nl

<https://doi.org/10.1007/s10853-024-09611-7>

## GRAPHICAL ABSTRACT



## Introduction

The automotive industry has been on the forefront of the search for new high-strength steel grades for decades. With the development of third-generation advanced high-strength steels (AHSS), the industry seeks to combine high strength with high ductility at a low cost. Doing so allows for creating more light-weight vehicles in order to reduce CO<sub>2</sub> emissions without compromising on passenger safety [1–4]. However, AHSS are especially vulnerable to hydrogen embrittlement (HE) because their microstructural features, such as high grain boundary densities, inter-phase boundaries and strain-induced martensite, are significantly affected by hydrogen [5–9]. In the worst

case, HE can manifest itself as sudden premature failure of parts.

One possible solution to HE that has received much attention is the use of carbides precipitated in the matrix as both a strengthening mechanism and a trap for hydrogen [10–18]. Carbides are associated with high activation energies,  $E_A$ , for hydrogen to leave specific traps and occupy different sites [19]. High activation energies decrease the overall concentration of diffusible hydrogen, which has been shown to be the main contributor to HE because it can diffuse towards critical areas in the microstructure around room temperature [11–13, 20, 21]. These critical areas can, for example, be interfaces [22] or crack tips [23], where the hydrogen contributes to crack initiation or growth,

**Table 1** Overview of different activation energies obtained from literature, converted to kJ/mol (1 eV = 96.5 kJ/mol)

| Carbide | Coherency and type of trap            | $E_A$ [kJ/mol]             | Type of study |
|---------|---------------------------------------|----------------------------|---------------|
| TiC     | Coherent precipitates                 | 42–59 [18, 24, 25]         | Experimental  |
|         | Coherent (Interface C-vacancy)        | 99–103 [29, 33]            | Numerical     |
|         | Semi-coherent (Interface dislocation) | 55.8 [17]                  | Experimental  |
|         |                                       | 48 [27]                    | Numerical     |
|         | Incoherent precipitates               | 53–145 [16, 39, 40]        | Experimental  |
|         | Bulk C-vacancy                        | 105–113 [29, 30]           | Numerical     |
| VC      |                                       | 80–90 [14, 17]             | Experimental  |
|         | Coherent (Interface C-vacancy)        | 37–56 [29, 32, 33]         | Numerical     |
|         |                                       | 60 [31]                    | Experimental  |
|         | Semi-coherent (Interface)             | 52–58 [12]                 | Experimental  |
|         | Bulk C-vacancy                        | 3–116 [29, 30, 36, 37, 41] | Numerical     |
|         | 62–67 [12]                            | Experimental               |               |

resulting in HE. Hydrogen traps associated with precipitates have been shown to have a wide range of activation energies. These vary not only between different precipitate types, but also within each type, predominantly with the precipitate size and as a consequence its coherency with the matrix.

Two of the most frequently studied precipitate types are titanium and vanadium carbides. Table 1 lists several values for hydrogen activation energies associated with different locations in these precipitates. TiC precipitates that are coherent with the matrix were experimentally found to have the lowest activation energies, ranging from 42 to 59 kJ/mol, which are attributed to traps on the interface between coherent TiC and the matrix [24, 25]. When the TiC precipitates reach a size of approximately 4.2 nm, the lattice mismatch between the precipitate and the matrix necessitates the creation of misfit dislocations on the precipitate/matrix interface [26]. These dislocations can also trap hydrogen and have been shown both experimentally and numerically to have activation energies very similar to the coherent interface [17, 27]. Eventually precipitates grow to become fully incoherent with the matrix. These TiC precipitates have been shown to strongly trap hydrogen [14], with an experimentally measured activation energy of up to 145 kJ/mol [16]. Debate is still ongoing, however, about where exactly hydrogen is trapped in these carbides. Atom probe observations by Takahashi et al. [28] suggest trapping at the interface of semi-coherent carbides. Interface trapping is also suggested by several other authors in studies on larger incoherent precipitates [16, 24]. These authors observe a reduction in trapped hydrogen with increasing precipitate size as a result of a reduction in total interface area. However, Wei et al. instead postulate that the amount of hydrogen trapped in TiC corresponds to their total volume [17]. This last finding is supported by a recent study by Vandewalle et al. who assume trapping to happen mainly at carbon vacancies in the bulk of incoherent TiC precipitates based on the larger equilibrium C-vacancy content in the bulk relative to the interface [14]. Numerical studies agree that C-vacancies in bulk TiC form good hydrogen traps, with activation energies ranging from 105 to 113 kJ/mol [29, 30]. Clearly, further investigation is required to identify the actual trapping site of H in incoherent TiC precipitates.

For VC precipitates, there is more consensus on the nature of hydrogen trapping. Malard et al. performed neutron scattering experiments that suggest hydrogen

trapping inside precipitates rather than on the interface [15]. This is confirmed by atom probe analysis that Takahashi et al. performed [31]. They conclude that hydrogen is stored inside the carbon vacancy on the coherent interface of small VC precipitates and find an activation energy of 60 kJ/mol. The same trapping site has been calculated numerically by several authors who find activation energies between 37 and 56 kJ/mol [32, 33]. Incoherent vanadium carbides have been shown to have an abundance of carbon vacancies and in fact often have a different stoichiometry such as  $V_4C_3$  or  $V_6C_5$  [34, 35]. This abundance of vacancies creates many possible sites for hydrogen trapping. Kawakami and Matsumiya calculate an activation energy of 116 kJ/mol [36] for C-vacancies in incoherent vanadium carbides, which is a high value compared to recent studies that find between 3 and 36 kJ/mol [29, 30, 37]. These values are rather low, but could be improved by doping the precipitates with transition metals [38]. On the other hand, an experimental study by Depover et al. attributes activation energies of 62–67 kJ/mol to the same traps [12]. Overall, the amount of studies in literature that focus on hydrogen trapping in vanadium carbides is rather limited compared to those that study titanium carbides. To the best of the authors' knowledge, no direct evidence of trapping in incoherent vanadium carbides has been found.

Needless to say, titanium and vanadium carbides provide an interesting opportunity for study of their effects on HE. Several approaches have been taken in the literature. The most common approach is to charge a steel containing the carbides of interest using electrochemical methods at room temperature [11, 12, 18, 40]. These studies, however, fail to charge hydrogen into the bulk of incoherent precipitates since the incoherent interface creates a diffusion boundary that cannot be overcome at room temperature [12, 16, 17]. The alternative is to charge steel with hydrogen during an annealing treatment in a hydrogen-containing atmosphere. This charging method is especially relevant to study hydrogen absorption during steel production stages such as hot-rolling or galvanising, as well as the performance of steels in hydrogen storage and transport applications. However, studies that used this method of high temperature gaseous hydrogen charging mostly performed them only on large semi- or incoherent carbides [14, 16, 18]. While these precipitates enhance hydrogen trapping capacity, smaller carbides are preferred as a strengthening mechanism in

steels [18, 31, 42, 43], so a trade-off between precipitate size and trapping capacity is likely required to achieve the best overall performance. A clear knowledge gap exists on the hydrogen trapping capacity of coherent or semi-coherent carbides and the effect thereof on the HE of their steels after high-temperature charging. Therefore, this work aims to investigate the effect of the precipitate size and coherency on the hydrogen absorption and embrittlement of the TiC and VC steels after hydrogenation in a high temperature gaseous hydrogen environment.

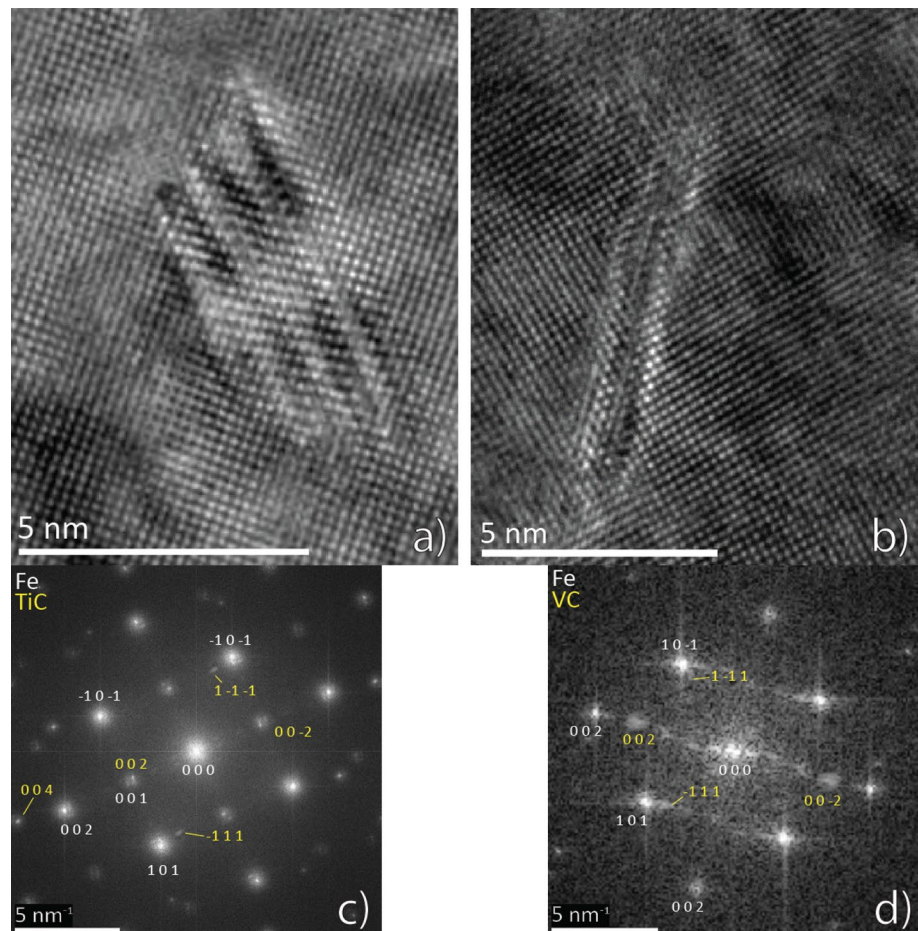
## Materials and methods

Two experimental single-phase ferritic high-strength low-alloy (HSLA) steels containing either titanium or vanadium carbides were cast by Tata Steel in IJmuiden for use in this research. The compositions, shown in Table 2, were chosen for maximum precipitation of TiC and VC. The Ti:C and V:C atomic ratios were matched as close to 1:1 as possible to achieve this. The as-received (AR) materials from Tata Steel were fully austenised before being hot rolled to a thickness of 3.5 mm. The slabs were cooled quickly to 630 °C after hot rolling and then subsequently cooled in a furnace to replicate slow coil cooling speeds. Hot rolling took

**Table 2** Summarised alloy contents of the TiC and VC alloys in weight %, determined using X-Ray Fluorescence (XRF)

| Alloy type | C    | Mn  | Al   | Si   | Ti   | V    | Trace elements | Balance Fe |
|------------|------|-----|------|------|------|------|----------------|------------|
| TiC        | 0.07 | 1.7 | 0.01 | 0.01 | 0.30 | –    | 0.04           | 97.8       |
| VC         | 0.07 | 1.8 | 0.01 | 0.02 | –    | 0.31 | 0.03           | 97.8       |

**Figure 1** TEM images of small precipitates in the as-received **a** TiC and **b** VC alloys. **c** and **d** Show the fast Fourier transform (FFT) image analyses of the images in **(a)** and **(b)**, respectively. Zone axis  $\langle 110 \rangle_{\text{carbide}} // \langle 010 \rangle_{\text{ferrite}}$  was used, which shows that  $\{001\}_{\text{carbide}} // \{001\}_{\text{ferrite}}$  according to the Baker–Nutting orientation relationship (OR).



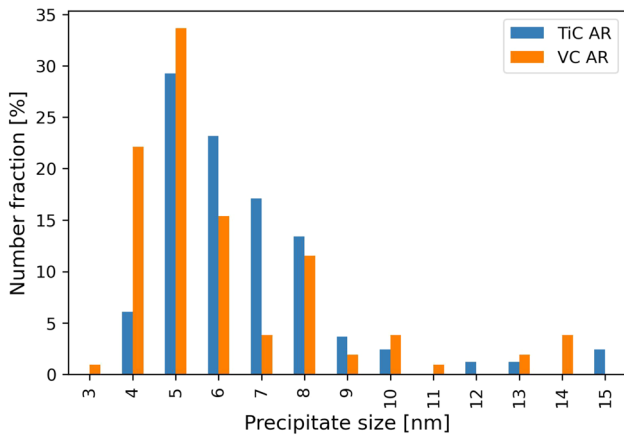


**Figure 2** Normalised TiC and VC precipitate size distributions in the AR alloys. Sizes are the average ( $\sqrt{\text{length} * \text{width}}$ ) sizes of platelet-shaped precipitates.

place entirely in the austenitic region (above Ar3) with the austenite-to-ferrite phase transformation and precipitation nucleation and growth in the ferrite phase starting from the fast cooling and continuing up to the initial residence period in the furnace set at 630 °C. Both microstructures are fully ferritic except for the second-phase precipitates.

Figure 1 shows Transmission Electron Microscopy (TEM) images of the TiC and VC precipitates in AR state. The TiC precipitates were found to be platelets with an average width of 6 nm and a thickness of 2 nm. The VC precipitates also appear as platelets, with a similar width but a smaller thickness of about 1 nm. An overview of the size distribution of precipitates in both compositions is given in Fig. 2. As can be observed in this figure, some larger precipitates were already present in both steels, but they only occur sparingly. Furthermore, both these precipitate types were found to comply with the Baker–Nutting orientation relationship (OR) ( $\{001\}_{\text{carbide}} // \{001\}_{\text{ferrite}}$  and  $\langle 110 \rangle_{\text{carbide}} // \langle 010 \rangle_{\text{ferrite}}$ ) between the precipitate and the matrix.

The steels were subjected to four different annealing heat treatments for this research. The main reason for these treatments was to grow the precipitates. Austenite start temperatures (A1) were determined as 729 °C for the TiC alloy and 696 °C for the VC alloy using the Thermo-Calc software package [44]. Ioannidou et al. studied the same VC composition and find a similar A1 temperature as well as no austenite formation after holding at 650 °C [45]. Following their approach, and in order limit grain growth and possible precipitate

dissolution, heat treatment temperatures were kept below the A1 temperatures and all heat treatments were performed at 700 °C for the TiC alloy and 650 °C for the VC alloy. To grow the precipitates to different sizes, heat treatment durations of both 2 h and 20 h were used. These times exclude a 5 °C/min heat up and a furnace limited cooling down ( $\pm 1$  °C/min). The second reason for utilising heat treatments was to charge the precipitates with hydrogen, to which end both heat treatments were also performed in a pure hydrogen atmosphere. The short 2 h heat treatments were performed in H<sub>2</sub> gas for the full duration. The long 20 h treatments were performed in N<sub>2</sub> for 18 h, followed by H<sub>2</sub> for 2 h. Only the last 2 h and the cooling down were performed in hydrogen for these treatments to exclude any effect of the gas on precipitate growth during the first 18 h. Lastly, both heat treatment durations were also performed in pure N<sub>2</sub> as a reference. Table 3 gives a concise overview of the heat treatments and how they will be designated throughout this paper. Before heat treatment, the surface of each specimen was sanded up to P1000 grit to create a repeatable surface finish.

**Microstructural characterisation**

After heat treatment, some specimens were prepared for microstructural analysis. Samples were cut and polished up to a 1 µm diamond finish for hardness measurements and scanning electron microscopy (SEM). Macro-hardness measurements were performed on an automatic Vickers hardness testing machine. The HV2 was recorded for all heat treatment conditions, where indents were at least 100 µm in size diagonally to be spaced over multiple grains. Extra OPS 0.04 µm finishing was performed for electron backscattering diffraction (EBSD) measurements.

**Table 3** An overview of different heat treatments used in this study and their designation throughout this article. All heat treatments were performed at 700 °C for the TiC alloy and 650 °C for the VC alloy

| Heat Treatment                                 | Designation                    |
|--|--------------------------------|
| 2 h in N <sub>2</sub>                          | SN (short nitrogen)            |
| 2 h in H <sub>2</sub>                          | SH (short hydrogen)            |
| 20 h in N <sub>2</sub>                         | LN (long nitrogen)             |
| 18 h in N <sub>2</sub> + 2 h in H <sub>2</sub> | LNH (long nitrogen + hydrogen) |

EBSD analysis was used to obtain an accurate grain size distribution, where only boundaries with an angle of more than 5 degrees were considered. Analysis was performed on a Thermo Fisher Scientific™ Helios™ G4 PFIB UXe SEM equipped with an EBSD sensor. In each case, mappings were made at an accelerating voltage of 20 kV, a current of 3.2 nA and a step size of 0.085  $\mu\text{m}$ .

Furthermore, TEM analysis was used to characterise the precipitates in both microstructures. Specimens were manually polished to 30  $\mu\text{m}$  thickness, followed by  $\text{Ar}^+$  ion milling to electron transparency. A Thermo Fisher Scientific™ Cs corrected cubed Titan™ was used, operating at 300 kV. For elemental analysis in STEM mode, the super-X detector in the ChemiSTEM™ configuration was employed, and TEM images were collected on a Ceta™ 16 M camera.

Lastly, Secondary Ion Mass Spectrometry (SIMS) imaging was employed to observe hydrogen trapping in larger TiC and VC precipitates present in the LNH heat treatment conditions. For SIMS analysis, samples of 1  $\text{cm}^2$  cross-sectional area were embedded in conductive resin and polished up to an OPS 0.04  $\mu\text{m}$  finish. SIMS analysis was carried out using high vacuum SCIOS-SIMS which is an instrument based on Thermo Fisher Scientific™ FIB-SEM platform with a magnetic sector mass spectrometer [46]. The mass spectrometer was developed in-house by Advanced Instrumentation for Nano Analytics (AINA) group of Luxembourg Institute of Science and Technology (LIST). The instrument uses  $^{69}\text{Ga}^+$  primary ions and has a mass resolving power ( $M/\Delta M$ ) of 400 [46]. It uses four channeltron detectors for mass filtered signal detection. In this work, the samples were biased to  $-500$  V in negative mode to extract  $^1\text{H}^-$  secondary ions and to  $+500$  V in positive mode to extract  $^{48}\text{Ti}^+$  and  $^{51}\text{V}^+$  secondary ions from the sample. The FIB was operated at an acceleration voltage of 30 kV and probe current of 50 pA. The background intensity in  $^1\text{H}^-$  SIMS images is slightly high due to the high vacuum (not UHV) condition of the instrument which results in the presence of higher amounts of hydrogen in the residual gas inside the chamber (e.g., humidity) [47].

### Thermal desorption spectroscopy

Thermal Desorption Spectroscopy (TDS) equipment was used to analyse the amount of absorbed hydrogen in the specimens. This was done on a Bruker

G8 Galileo device equipped with an IR07 infrared furnace that allows for custom temperature ramping while continuously measuring the desorbed hydrogen flux using a thermal conductivity detector. TDS was performed on steel specimens of  $2 \times 20 \times 110$  mm in size, which were first sanded with P1200 sandpaper to remove any oxidation layer and create a reproducible surface finish for desorption. Each combination of steel type and heat treatment was measured at least 3 times with different heating rates, namely 1, 0.66 and 0.33  $^\circ\text{C}/\text{s}$ . All measurements were performed over a range of 40–900  $^\circ\text{C}$ .

Performing TDS measurements at different heating rates allows for fitting of peak temperatures according to the simplified Kissinger equation [48]:

$$\frac{d \ln(\phi/T_{\max}^2)}{d(1/T_{\max})} = -\frac{E_A}{R} \quad (1)$$

In this equation,  $T_{\max}$  is the peak temperature of a specific H desorption peak in K,  $\phi$  is the heating rate in K/s,  $R$  is the universal gas constant  $8.3415 \text{ J} \cdot \text{K}^{-1} \cdot \text{mol}^{-1}$ , and  $E_A$  is the activation energy for hydrogen desorption of the specific hydrogen trap in kJ/mol. By fitting  $\ln(\phi/T_{\max}^2)$  to  $(1/T_{\max})$ ,  $E_A$  can be inferred from the slope.

### Mechanical characterisation

Five tensile specimens were prepared and subsequently subjected to each heat treatment condition for mechanical characterisation in a Slow Strain Rate Tensile (SSRT) test. Figure 3 displays the specimen geometry. The specimens were all machined perpendicular to the rolling direction of the steel sheets. Before each test, the specimen was sanded up to a P1200 grit finish to remove any oxide layer

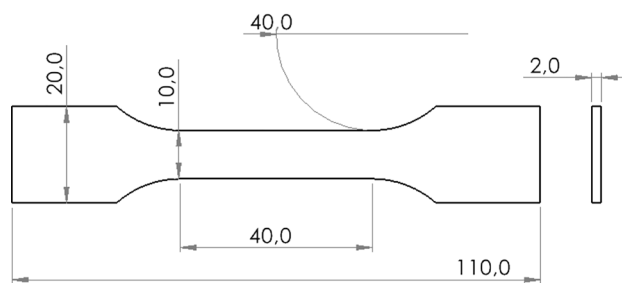


**Figure 3** Drawing of the tensile specimen geometry used for SSRT testing. Dimensions are in mm.

and realise a surface finish similar to that of the TDS specimens. The tests consist of a constant crosshead displacement of 4.5 mm/h until fracture, which corresponds to an original strain rate of  $3 \cdot 10^{-5} \text{ s}^{-1}$  in the gauge section. This strain rate was chosen to allow for sufficient hydrogen diffusion throughout the specimen during the test according to ASTM G142 and G129 [49, 50]. The tests were performed on a Zwick Z100 universal tensile tester.

## Results and discussion

### Grain size evolution

Each sample condition was prepared for EBSD analysis of the grain structure in order to characterise the grain size evolution after all heat treatment conditions. Areas containing several hundreds of grains were measured. Representative images of the both

steels after conditions SN and LN (designated  $VC_{SN}$ ,  $VC_{LN}$ ,  $TiC_{SN}$  and  $TiC_{LN}$ , respectively) are shown in Fig. 4. Microstructures resulting from the short 2 h heat treatment conditions still show some degree of deformation of the lattice as a result of the hot-rolling process. This is eliminated after the long heat treatment of 20 h. X-Ray Diffraction (XRD) measurements confirmed the microstructures after all heat treatment conditions to be fully ferritic. It was found that grain growth during the annealing cycles is limited, and the microstructures of both alloys after long heat treatments are not significantly different from those after short heat treatment as a result of grain boundary pinning by the nano-carbides. The grains are non-equiaxed and widespread in areas ranging from  $< 1 \mu\text{m}^2$  to occasional grains with areas of  $> 100 \mu\text{m}^2$ . Smallest, average and largest grain areas were obtained from the EBSD images and are listed in Table 4 as advised by ASTM E1181 for a random grain size distribution of large range [51]. A grain area of  $0.1 \mu\text{m}^2$  was chosen

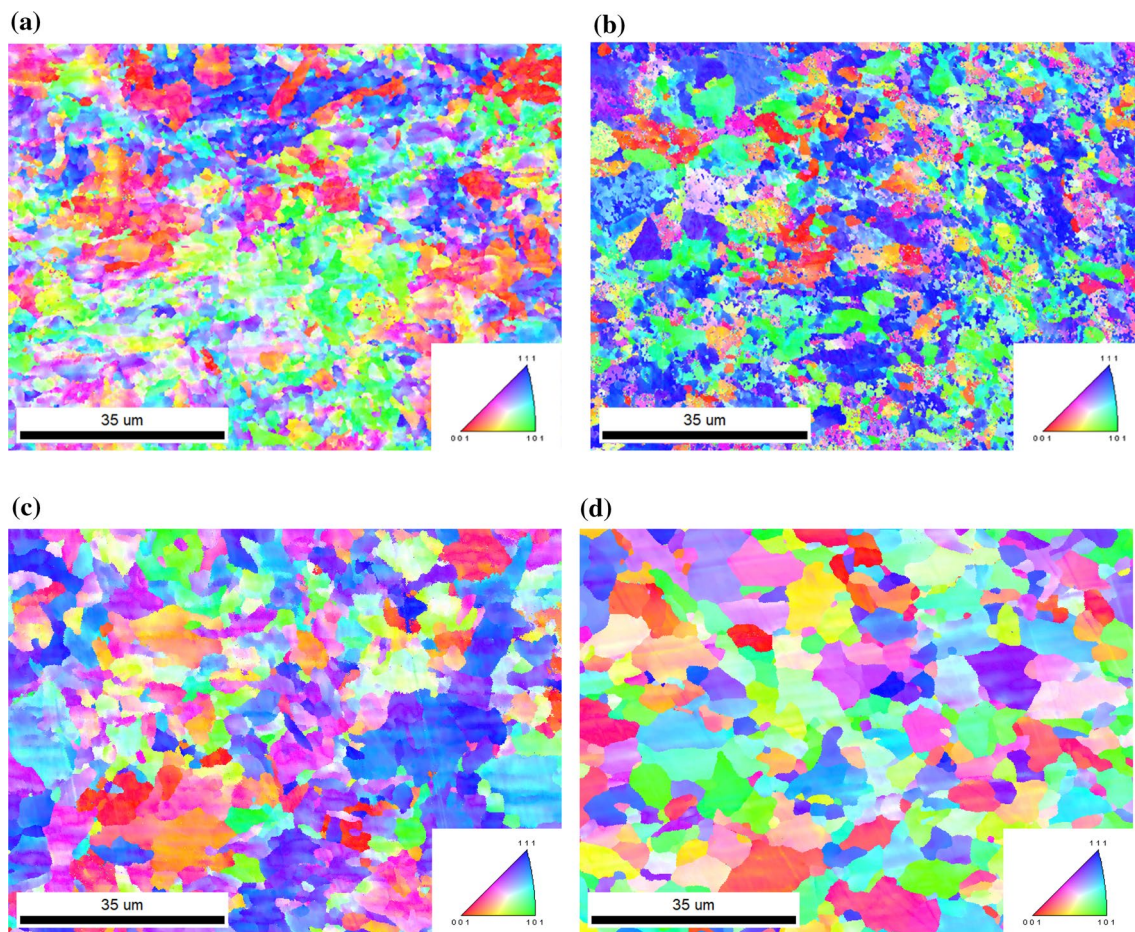


**Figure 4** Inverse pole figures of the **a**  $TiC_{SN}$ , **b**  $TiC_{LN}$ , **c**  $VC_{SN}$  and **d**  $VC_{LN}$  conditions, obtained using the OIM Analysis™ software.

as the cut-off point where individual grains can be accurately distinguished from noise with the chosen EBSD step size of 85 nm. Only little grain growth is observed in the TiC alloy even after the long 20 h heat treatments. Any reduction in strength as a result of the heat treatments can therefore be attributed to precipitate growth and the resultant over-aging of the microstructure. In contrast, the average grain size in the VC alloy roughly doubles after the 20 h compared to 2 h so an influence of grain growth on strength reduction is expected. Since it has been shown in the literature that high-temperature hydrogen charging does not fill grain boundaries [14, 16, 26], an influence of varying grain sizes on HE is not expected.

### Precipitate growth

After TEM analysis of all heat treatment conditions, the acquired images were scanned for precipitates. The average size ( $\sqrt{\text{length} * \text{width}}$ ) of all visible precipitates was manually measured from these images, of which the smallest, average and largest ones are listed in Table 4. The full distributions are displayed in Fig. 5a for condition SH and in Fig. 5b for LNH. Distributions in conditions SN were confirmed to be identical to that in SH for both alloys, as well as condition LN to that for LNH. It becomes apparent from Fig. 5a that the TiC precipitates adhere to an approximate normal distribution around an average of 10 nm. The VC precipitates, on the other hand, seem to be somewhat smaller in size. The largest fraction of them lies around an average of 5 nm, with some occurrences between 20 and 30 nm in size. Both precipitate types

thus show some growth after a short heat treatment of 2 h when compared to the AR state, although the titanium carbides show more coarsening after this short duration. The distributions differ after the long 20 h treatment, for which figure 6 illustrates some precipitate occurrences. The TiC distribution still shows a large fraction of carbides around a size of 10–15 nm, although some larger precipitates now start to arise that grow to 20 nm or more. The VC distribution shows a larger fraction of precipitates in the 20–30 nm size than the TiC, and almost all those smaller than 10 nm have disappeared. Figure 5b also shows incidental occurrence of precipitates larger than 100 nm in size for the TiC alloy. In fact, these precipitates were observed for both the VC and TiC alloys in all heat treatment conditions, as well as in the AR state. TEM analysis often overlooks them since their spacing is large compared to the analysed area, but through SEM and SIMS observations it was shown that they exist in all conditions and do not grow in size considerably even after the long heat treatments. The amount of large incoherent precipitates in the TiC alloy was higher than that in the VC alloy. The average TiC precipitate size in Table 4 is therefore skewed to a larger average size than the VC precipitates, even though Fig. 5b shows the  $\text{TiC}_{\text{LNH}}$  precipitates to be smaller than the  $\text{VC}_{\text{LNH}}$ . Lastly, it was observed that carbides in the VC alloy preferentially grow on grain boundaries. This is shown in Fig. 6.

Wei et al. state that the critical size for TiC precipitates with the Baker–Nutting orientation to be coherent is 4.2 nm across the broad surface [26]. Therefore, only the fraction of carbides that was measured to be

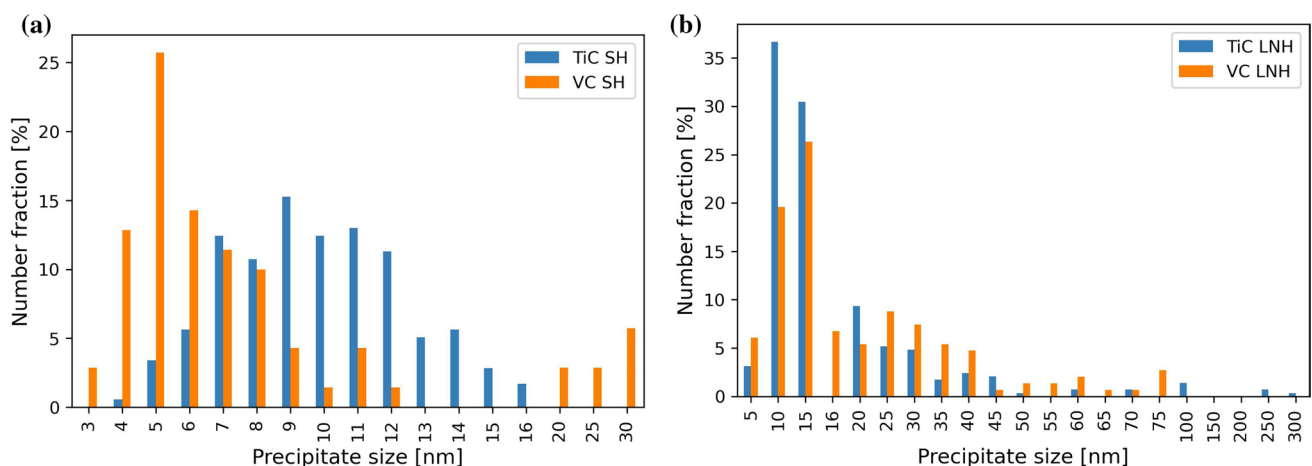


**Figure 5** Normalised precipitate size distributions for both alloys in conditions **a** SH and **b** LNH.



**Figure 6** High-Angle Annular Dark-Field (HAADF) and Energy Dispersive X-Ray (EDX) images of **a** 5–30 nm and **b** 350 nm TiC precipitates, and **c** 10–90 nm and **d** a group of 50–90 nm VC precipitates found in the specimens TiC<sub>LNH</sub> and VC<sub>LNH</sub>, respectively.

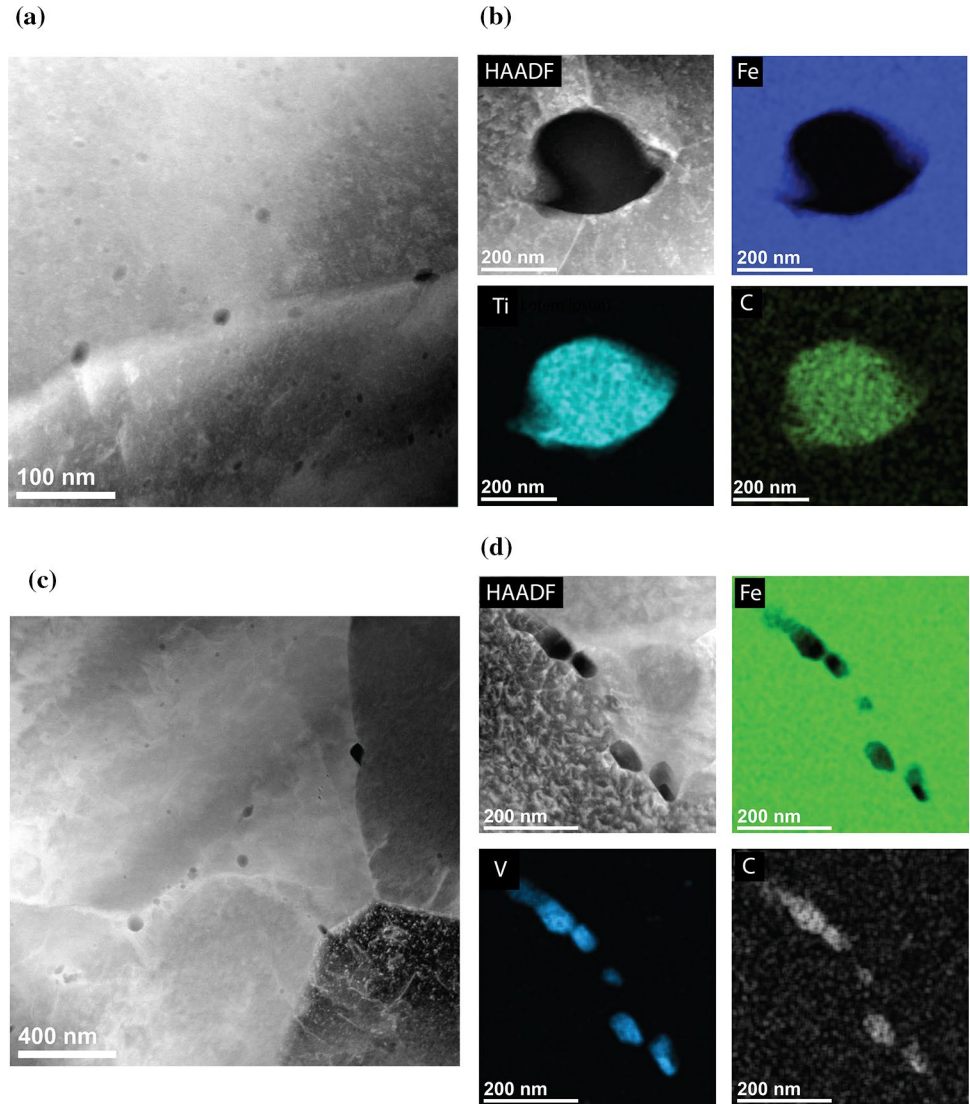


**Table 4** An overview table with microstructural details for all heat treatment conditions. Grain areas were obtained from EBSD results; precipitate sizes were characterised using TEM

|     | HT  | Hardness HV2 | Grain area [ $\mu\text{m}^2$ ] |         |      | Precipitate size [nm] |         |      |
|-----|-----|--------------|--------------------------------|---------|------|-----------------------|---------|------|
|     |     |              | Low                            | Average | High | Low                   | Average | High |
| TiC | AR  | 267 ± 1.9    | –                              | –       | –    | 2.9                   | 5.7     | 60   |
|     | SN  | 272 ± 3.1    | 0.1                            | 3.8     | 160  | 2.8                   | 8.6     | 290  |
|     | SH  | 270 ± 2.7    | 0.1                            | 2.5     | 159  | 3.2                   | 6.5     | 140  |
|     | LN  | 238 ± 1.6    | 0.1                            | 5.0     | 192  | 5.7                   | 30.3    | 235  |
|     | LNH | 223 ± 0.4    | 0.1                            | 4.0     | 189  | 3.6                   | 21.7    | 223  |
| VC  | AR  | 261 ± 2.4    | –                              | –       | –    | 2.6                   | 6.1     | 150  |
|     | SN  | 241 ± 1.2    | 0.1                            | 12.5    | 223  | 3.8                   | 9.9     | 522  |
|     | SH  | 246 ± 1.0    | 0.1                            | 10.8    | 243  | 3.6                   | 7.9     | 470  |
|     | LN  | 230 ± 0.7    | 0.1                            | 24.9    | 231  | 2.5                   | 17.6    | 349  |
|     | LNH | 222 ± 1.2    | 0.1                            | 23.3    | 299  | 3.5                   | 17.4    | 294  |

smaller than 5 nm could be coherent across the interface. Table 4 shows that precipitates smaller than this size were observed in the AR as well as the SN and SH heat treatments. However, this is only a small fraction of all precipitates as can be observed from Figs. 2 and 5a. Therefore, most of the precipitates will instead be semi-coherent with the steel matrix. After the 20 h heat treatments, the small TiC precipitates are considered to be exclusively semi-coherent, while the medium- and larger-sized ones are incoherent with the matrix. VC precipitates have a lattice constant that is closer to that of the steel lattice, so the critical size for coherency is slightly larger. Takahashi et al. observe small platelike VC precipitates with a thickness of 2–5 nm and a length of approximately 20 nm to be mostly coherent with the matrix, except for misfit dislocation around the curved sides [31]. This is larger than the sizes found for the 2 h heat treatments in this research, so the small VC precipitates can be considered coherent with the matrix at this size. After the 20 h heat treatment, Fig. 6c shows medium-sized vanadium carbides to be more globular in shape. This is an indication that the surface is no longer coherent with the matrix and will instead have become semi-coherent or fully incoherent, though it becomes clear from Fig. 5b that some smaller precipitates still remain coherent. It is known that incoherent vanadium carbide precipitates do not usually have a 1:1 stoichiometry but rather exist as  $V_4C_3$  or  $V_6C_5$  structures with a high carbon vacancy content [34, 35]. A varying V–C ratio was also found in elemental analysis during STEM measurements, which confirms large amounts of carbon vacancies in incoherent VC precipitates. The TiC precipitates also showed the presence of carbon-vacancies, but only at precipitate sizes of > 100 nm.

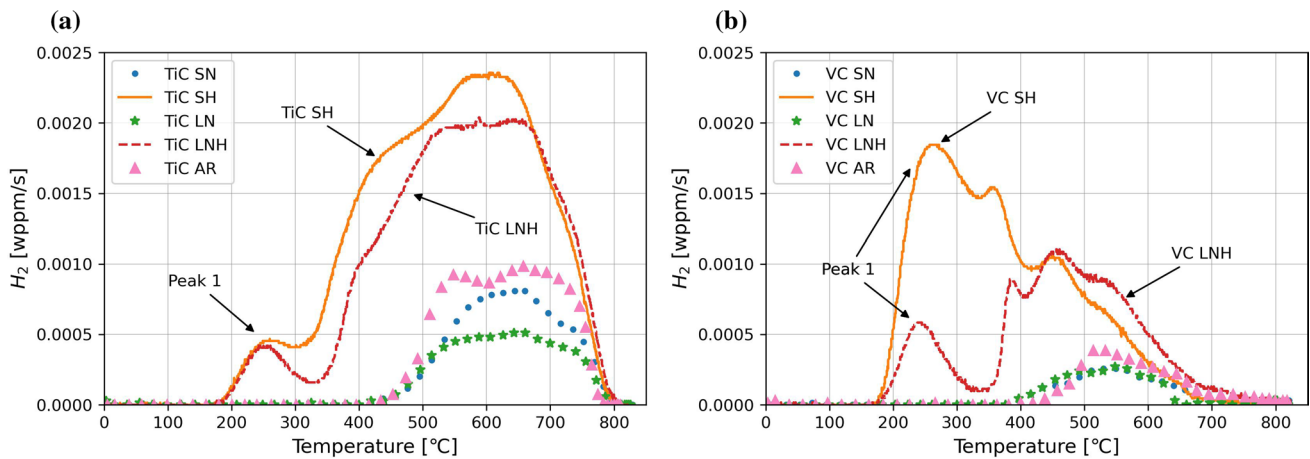


**Figure 7** TDS spectra obtained at a heating rate of 1 °C/s for all conditions in **a** the TiC alloy and **b** the VC alloy.

**Table 5** Overview of hydrogen contents in weight part per million (wppm) for all heat treatment conditions

| Heat Treatment   | TiC $H_2$ [wppm] | VC $H_2$ [wppm]   |
|------------------|------------------|-------------------|
| As-received (AR) | $0.30 \pm 0.03$  | $0.09 \pm 0.03$   |
| SN               | $0.22 \pm 0.02$  | $0.06 \pm < 0.01$ |
| SH               | $0.91 \pm 0.03$  | $0.44 \pm 0.07$   |
| LN               | $0.17 \pm 0.02$  | $0.06 \pm < 0.01$ |
| LNH              | $0.70 \pm 0.04$  | $0.28 \pm 0.03$   |

Supplementary figures S1, S2 and S3 show examples of EDX maps and line scans to illustrate the V:C and Ti:C ratios in selected precipitates.

### Effect on hydrogen absorption

TDS was used to analyse the hydrogen absorption in all conditions. Table 5 lists the total amount of hydrogen trapped in each set of heat treatments. A first observation to be made is that the AR materials already contain a small amount of hydrogen, which is most likely a consequence of hydrogen absorption from water vapour during hot rolling, which has been shown to charge TiC precipitates by Wei et al. [26]. The TiC alloy contains the most hydrogen, with 0.30 wppm on average, compared to 0.09 wppm in the AR VC steel. It can also be observed that the heat treatments in a pure  $N_2$  environment decrease the total hydrogen content relative to that in the AR state. This is to be expected since if there is no additional hydrogen present to charge the samples during the heat treatment, hydrogen will be desorbed instead. The VC alloy contains less hydrogen overall than the TiC alloy,

although the trends are similar. The hydrogen content in the TiC steel is reduced to 0.22 and 0.17 wppm in the SN and LN heat treatments, respectively. The hydrogen content in the VC steel is slightly reduced to 0.06 wppm after the SN heat treatment, which does not decrease further after the LN heat treatment.

The TiC<sub>SH</sub> condition contains a hydrogen content of 0.91 wppm, compared to 0.70 in condition TiC<sub>LNH</sub>. This difference can most likely be attributed to a difference in precipitate size distribution. A similar effect can be observed in the VC alloy, which contains 0.44 wppm in condition VC<sub>SH</sub> and 0.28 in condition VC<sub>LNH</sub>. The desorption spectra in Fig. 7 show that although the hydrogen trap distribution is very similar between the two heat treatment conditions in the TiC alloy, it differs significantly in the VC alloy. The lowest temperature peak (Peak 1 in Fig. 7b) decreases in size significantly after a long heat treatment duration, whereas the other peaks stay relatively similar in size. Moreover, the high-temperature peaks above 400 °C contain much less hydrogen than their counterparts in the TiC alloy. This suggests less overall H trapping in the incoherent VC precipitates, but the smaller amount of incoherent VC compared to TiC precipitates also plays a role. The fact that the hydrogen desorption spectra level off around 700 °C in the VC alloy compared to 800 °C in the TiC alloy suggests lower energy trapping for the incoherent VC precipitates.

### Hydrogen trapping strength

Other than the desorption spectra shown in Fig. 7 measured at 1 °C/s, all conditions were also tested at heating rates of 0.66 and 0.33 °C/s. This was done to allow fitting of peak temperatures according to the simplified Kissinger's equation (Eq. 1). To obtain the peak temperatures, the desorption spectra of each heating rate were fit to 4 skewed Gaussian peaks using the Python LMFIT package. The deconvoluted curves for Peak 1 in all VC<sub>SH</sub> heating rates and the resulting plot to calculate  $E_A$  are displayed in Figure S4 for illustration. Unfortunately, significant peak overlap above 300 °C made any realistic interpretation of trapping energies impossible. This is an issue also encountered by Vandewalle et al. [14] and Drexler et al. [52], who review the Kissinger theory and its applicability to overlapping peaks. They find that accurate validation of trapping energies for overlapping peaks can only be obtained if extra boundary conditions based on

**Table 6** Overview of the trapping energies obtained for Peak 1 in all hydrogen charged conditions

| HT Condition       | $E_A$ [kJ/mol] |
|--------------------|----------------|
| TiC <sub>SH</sub>  | 96 ± 2         |
| TiC <sub>LNH</sub> | 43 ± 3         |
| VC <sub>SH</sub>   | 54 ± 1         |
| VC <sub>LNH</sub>  | 72 ± 10        |

relative hydrogen trap occupancy are applied to the fitting method. Such knowledge was not obtained in this work. Therefore, further discussion and relation to trapping energies will be restricted to those obtained for the lowest temperature peaks, or Peak 1 as shown in Fig. 7 and listed in Table 6, since these peaks show sufficient separation from the rest of the spectrum for sound interpretation. None of these first peaks can be classified as a fully reversible trap, which is most commonly associated with trapping energies of < 30 kJ/mol [52, 53]. Instead, trapping energies range from strong to fully irreversible with trapping energies ranging between 43 and 96 kJ/mol.

## Origins of hydrogen trapping in TiC

### Origin of the first peak

Figure 7a shows that the desorption spectra for TiC after the short and long heat treatment durations look mostly similar. This suggests that the same traps are occupied inside the steel, but their relative occupancy differs. Firstly, it seems that the low-temperature peak remains almost identical in both conditions. In the literature, low-temperature trapping is frequently associated with coherent or semi-coherent precipitates. Direct observation of deuterium at TiC interfaces has been made by Takahashi et al. in atom probe studies, on precipitates that are similar in morphology to those observed in conditions TiC<sub>SN</sub> and TiC<sub>SH</sub> [28]. Deuterium was observed around the precipitate interface of the plate-like carbides, but not in the bulk, which suggests either interface misfit dislocations or interface C-vacancies as a possible trapping site. Wei et al. measure coherent TiC precipitates to have an overall activation energy of between 46 and 59 kJ/mol [18], but state in a different paper that the misfit dislocation on the semi-coherent interface of TiC has an activation energy of 56 kJ/mol [17]. A different study attributes an energy of 42 kJ/mol to the interface of incoherent precipitates [24], which is close to a value calculated in a separate atomistic study, that finds a maximum of

48 kJ/mol for a misfit dislocation [27]. Since a value of 43 kJ/mol was measured for the  $\text{TiC}_{\text{LNH}}$  condition in this research, it is reasonable to assume that the misfit dislocation is the origin of this trapping peak. However, this is in contrast to the value for Peak 1 in the  $\text{TiC}_{\text{SH}}$  condition, which was measured as 96 kJ/mol. This value is closer to values of 111 kJ/mol obtained by Zhang et al. [33] and 99 kJ/mol obtained from our previous research [29], where activation energies were calculated for a C-vacancy on a coherent TiC surface in BCC iron. An explanation why two different values could be measured is that there is a small fraction of precipitates after the 2 h heat treatment condition that is fully coherent with the matrix. These are most likely the precipitates in Fig. 5a with a size smaller than 5 nm. After a short heat treatment, hydrogen could be trapped here in C-vacancies on the coherent interface. These precipitates grow to a semi-coherent size after heat treatment conditions  $\text{TiC}_{\text{LN}}$  and  $\text{TiC}_{\text{LNH}}$  in which case the hydrogen is trapped in misfit dislocations instead of C-vacancies.

#### *Origin of the high-temperature peaks*

The high-temperature peaks in the TiC desorption spectra can be attributed to hydrogen trapping by incoherent precipitates, like the studies by Vandewalle et al. and Pérez-Escobar et al [14, 16]. A comparable study, which has similar TiC size distributions to those observed in this research, finds a reduced H absorption through electrochemical charging with increasing annealing time and consequently precipitate size [24]. They attribute this to trapping on the precipitate interface, which has a high activation energy and diffusion barrier and decreases with increasing precipitate size. This could explain that the spectrum for  $\text{TiC}_{\text{LNH}}$  shows less trapped hydrogen at peaks between 350 and 700 °C than that for  $\text{TiC}_{\text{SH}}$ . The same conclusion is also reached by other authors [16, 17, 26], although direct observations were not made. The highest temperature peaks at roughly 450 °C and above are expected to belong to traps inside the largest precipitates of size > 100 nm. In this study, these were seen to already be present in the AR material and remain relatively unchanged after heat treatment. Vandewalle et al. attribute an increased concentration of incoherent TiC precipitates to an increased hydrogen uptake in the peaks between 500 and 900 °C [14]. Since precipitates of this size are not changed significantly in this

research, the hydrogen uptake in these peaks stays relatively similar..

#### *Observation of trapping in incoherent TiC*

Vandewalle et al. assume trapping in bulk C-vacancies only [14], based on theoretical work by Di Stefano et al. who discuss hydrogen diffusion into the TiC bulk through continuous C-vacancy networks [27]. Incoherent TiC precipitates that have a continuous C-vacancy network throughout the bulk require a lower diffusion energy for hydrogen to migrate into the precipitate bulk than precipitates where C-vacancies are not connected but instead separated by interstitial sites. This creates a different hydrogen absorption behaviour per precipitate, even though the activation energy of the trap stays the same. Hydrogen trapping in incoherent TiC was directly observed in this study through SIMS imaging. Figure 8a and 8b shows hydrogen and titanium secondary ion maps, respectively, of the same area on the surface of a  $\text{TiC}_{\text{LNH}}$  sample. It can be observed from these images that not all of the titanium rich precipitates in Fig. 8b trap hydrogen identically. One precipitate appears to store hydrogen more in the bulk, whereas the others store more around the interface. This is highlighted especially in Fig. 9a, which shows a SIMS hydrogen map from a different area. The image shows that the hydrogen is localised around the circumference of these precipitates rather than over the entire bulk. Figure 8d shows a line profile along the white arrow in Fig. 8c. It is easy to see that, on the one hand, a significant amount of hydrogen is trapped in the precipitate, while on the other hand the hydrogen concentration inside the bulk is much lower than towards the interface. In fact it is similar to the level in the matrix. Hydrogen absorption in TiC precipitates scaling with surface area is refuted by the work of Pérez-Escobar et al. [16] and Wei et al. [54], who state that hydrogen absorption is proportional neither to precipitate surface area nor volume since they do not see a clear relation between increasing precipitate size and reducing hydrogen absorption. While no direct link to decreasing surface area can be made from this work, the TDS spectra show that the TiC alloy absorbs less hydrogen in the incoherent precipitates with increasing annealing time, while SIMS images show a higher concentration near the interface. This indicates that incoherent TiC preferentially traps hydrogen near the interface, although

**Figure 8** SIMS images of **a**  $^1\text{H}^-$  map and **b**  $^{48}\text{Ti}^+$  map over the same area of acquisition in the TiC-containing steel. Both the images were acquired using a beam current of 50 pA and a dwell time of 2.5 ms per pixel. The image resolution is  $256 \times 256$  for a field of view  $9 \mu\text{m} \times 9 \mu\text{m}$ . **c** Shows merged elemental maps of  $^1\text{H}^-$  (green) and  $^{48}\text{Ti}^+$  (red) and **d** Shows a line profile of the region indicated by white arrow in (c). The counts of the line profile diagram have been normalised for a qualitative comparison.

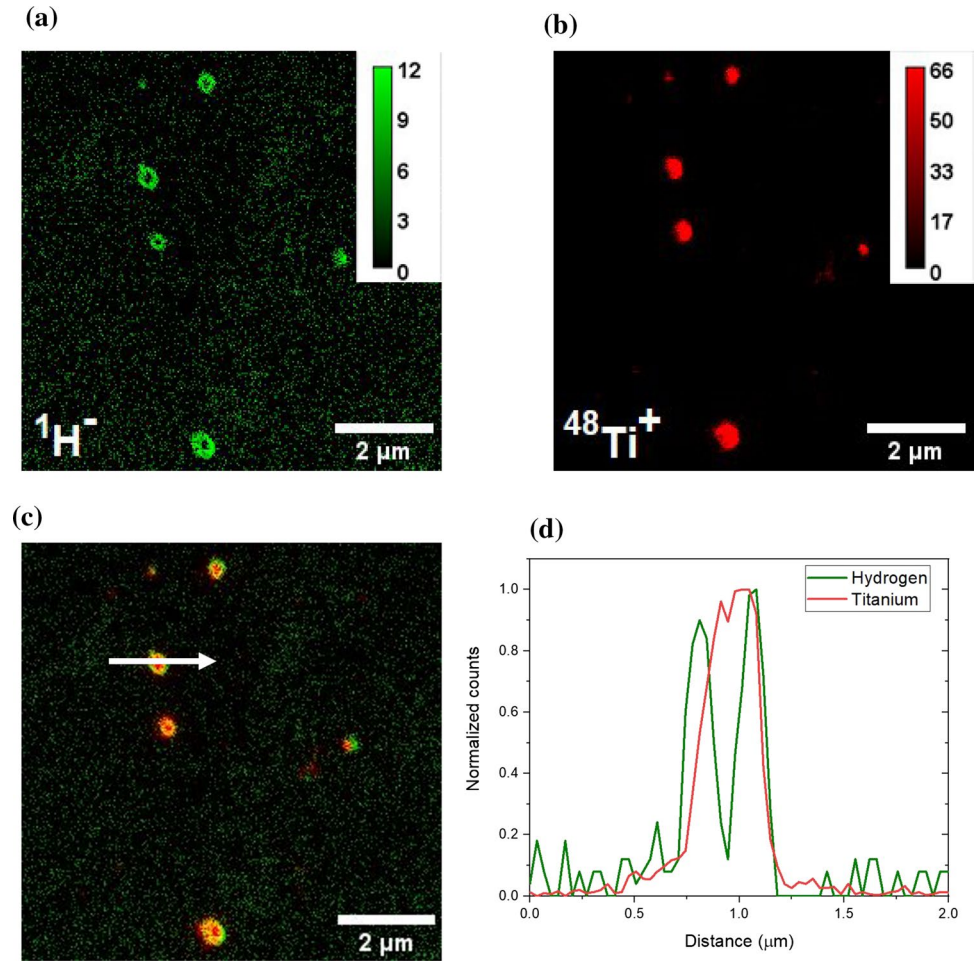
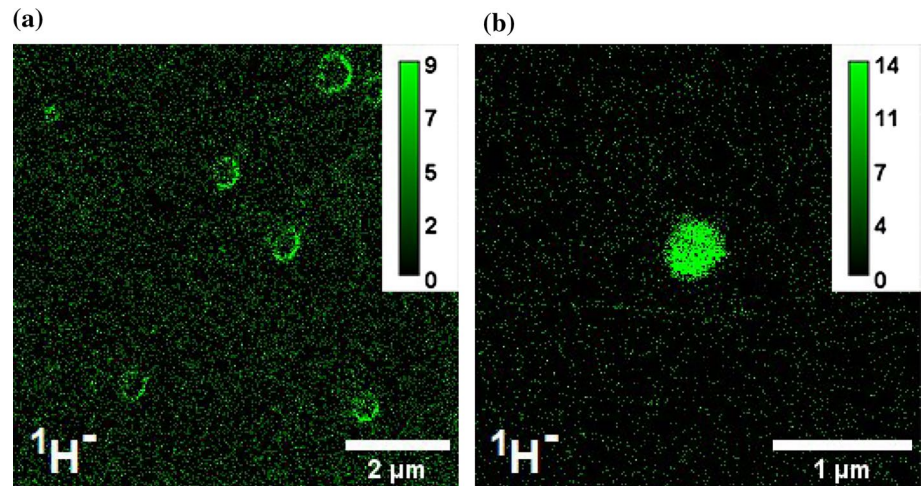


**Figure 9** Hydrogen maps obtained by SIMS analysis, showing **(a)** localisation around TiC precipitates and **(b)** trapping in a VC precipitate. Both the images were acquired using a beam current of 50 pA and dwell time 1 ms per pixel. **a** has a resolution of  $256 \times 256$  over a field of view  $9 \mu\text{m} \times 9 \mu\text{m}$  and **b** has a resolution of  $256 \times 256$  over a field of view  $3 \mu\text{m} \times 3 \mu\text{m}$ .



SIMS is not a suitable technique to definitely prove trapping on the interface.

It should be noted that the time between hydrogen charging and analysis was significant for these images, with hydrogen charging happening some months

before analysis. On the one hand, this shows that indeed these precipitates form very strong hydrogen traps. On the other hand, it does not clarify whether this distribution of hydrogen around the precipitate circumference is a result of hydrogen absorption during charging or desorption during storage. If fast diffusion through C-vacancy networks into TiC is assumed, off-stoichiometric precipitates with a high vacancy concentration would absorb more hydrogen over their entire bulk during the charging cycle, whereas precipitates with a lower vacancy concentration would trap most hydrogen near the interface. However, precipitates with a vacancy network allowing for fast diffusion would also release hydrogen more quickly during storage. Hydrogen release during storage is observed to be minimal, so the observation of hydrogen around the precipitate circumference is attributed to preferential trapping around the incoherent TiC/matrix interface. However, more analysis is required to fully validate this, including observations at different times after charging.

## Origins of hydrogen trapping in VC

### *Origin of the first peak*

The TDS spectra for VC<sub>SH</sub> and VC<sub>LNH</sub> show a stark difference in the amount of hydrogen trapped in the lowest temperature peak. Like the TiC alloy, this peak can most likely be attributed to the trapping in smaller VC carbides. As discussed previously, the VC precipitates are still largely in the coherent domain after a 2 h heat treatment. Since no misfit dislocations are present in this case, the likely hydrogen trap is the C-vacancy on the coherent interface. The activation energy for C-vacancies measured by Takahashi et al. is approximately 60 kJ/mol [31], which matches reasonably well with the trapping energies of 53 and 72 kJ/mol measured in this research for the conditions VC<sub>SH</sub> and VC<sub>LNH</sub>, respectively. Experimentally, Depover and Verbeken found an activation energy of 52 to 60 kJ/mol for V<sub>4</sub>C<sub>3</sub> carbides, but only up to a size of 20 nm after electrochemical hydrogen charging [12]. Numerical studies have found activation energies for the trap at a coherent interface C-vacancy of 36.7 [32], 55.9 [33] and 51 kJ/mol [29]. Since all of the values are similar to what was measured in this work, the low-temperature peak is attributed to the carbon vacancy on the coherent VC interface.

### *Origin of the high-temperature peaks*

After having grown during the long heat treatments, as shown in Fig. 6, most VC precipitates outgrow the coherent domain and become incoherent. The low-temperature peak therefore largely disappears in the VC<sub>LNH</sub> condition, as it did in the work by Depover and Verbeken [12]. At higher temperatures, however, the hydrogen uptake is slightly larger in the VC<sub>LNH</sub> condition than in the VC<sub>SH</sub> condition, which could be an effect of an increased amount of hydrogen trapped in the bulk of larger precipitates which increase in number with a longer heat treatment duration. To the authors' knowledge, no previous research has attempted high-temperature charging of VC precipitates, and as such no trapping energies have been found for them in the literature. Unfortunately, due to strong peak overlap, no reliable trapping energies for these traps could be found in this research. Nonetheless, the high-temperature peaks are attributed to trapping in carbon vacancies in the bulk of incoherent VC precipitates.

### *Observation of trapping in incoherent VC*

Figure 9b shows a SIMS hydrogen map of the VC<sub>LNH</sub> condition. The carbide can be seen to store hydrogen all throughout the bulk, contrary to the TiC carbides in Fig. 9a which predominantly stores hydrogen near the interface. A comparison of the hydrogen trapping locations in the SIMS images suggests that H trapping in VC precipitates should scale with volume. This is supported by the TDS curve from Fig. 7b, where the VC alloy stores more hydrogen at high temperatures after the longer treatment. Incoherent VC precipitates are therefore expected to be able to store more hydrogen overall than their TiC counterparts. However, since the total amount of incoherent vanadium carbides was much lower than that of the titanium carbides, this was not observed in this study.

### **Effect on mechanical behaviour**

SSRT tests were used to characterise the extent of HE for each alloy and heat treatment condition, of which the results are summarised in Table 7. Representative tensile curves for each of the heat treatment

**Table 7** Overview of the 0.2% proof yield strength  $\sigma_{y,0.2\%}$ , UTS and strain at break  $\epsilon_f$  for all heat treatment conditions. Errors are standard deviations

| Alloy | Heat Treatment | $\sigma_{y,0.2\%}$ [MPa] | UTS [MPa] | $\epsilon_f$ [%] |
|-------|----------------|--------------------------|-----------|------------------|
| TiC   | AR             | 698 ± 2                  | 804 ± 2   | 10.6 ± 0.39      |
|       | SN             | 638 ± 22                 | 740 ± 18  | 15.2 ± 0.35      |
|       | SH             | 624 ± 10                 | 727 ± 2   | 16.1 ± 0.53      |
|       | LN             | 533 ± 60                 | 650 ± 39  | 17.6 ± 0.50      |
|       | LNH            | 579 ± 57                 | 652 ± 27  | 18.5 ± 0.94      |
| VC    | AR             | 656 ± 7                  | 736 ± 2   | 10.0 ± 0.13      |
|       | SN             | 656 ± 7                  | 743 ± 7   | 16.5 ± 1.08      |
|       | SH             | 658 ± 10                 | 758 ± 4   | 17.1 ± 0.88      |
|       | LN             | 583 ± 6                  | 674 ± 12  | 18.4 ± 0.53      |
|       | LNH            | 567 ± 11                 | 658 ± 6   | 16.6 ± 1.24      |

conditions are shown in Fig. 10. A first observation to note is that even the short heat treatments in the TiC alloy decrease its strength compared to the AR condition while  $\epsilon_f$  is increased from 10.6 to 15.2 %. The long heat treatment in the TiC alloy further decreased both yield strength and UTS by approximately 10%.  $\epsilon_f$  is only increased slightly in these conditions, but because of a larger scatter in values it is not a conclusive increase. In the VC, the 2 h heat-treated samples do not show a reduction in strength compared to the AR condition, which is a result of limited precipitate growth after 2 h. It is only seen after the long heat treatments, where it drops by approximately 10–15 %. An increase in  $\epsilon_f$  from 10 to 16.5 % is observed in the short heat treatments compared to the as-received condition, but

once again the scatter increases after long heat treatments. Therefore, no conclusive statements about an increase or decrease can be given. In the TiC alloy, the change in mechanical behaviour between the 2 h and 20 h heat treatments can be explained by precipitate over-aging [43], since Table 4 shows that the grain size did not significantly increase even after the long heat treatment, while the precipitates were found to increase in size. In the VC alloy, the grain size did show an increase, which mean the reduction in strength is likely a combination of grain growth and precipitate over-aging.

Hydrogen embrittlement, which would become apparent as a reduction in  $\epsilon_f$  in the condition SH compared to SN, or LNH compared to LN, is not observed in any case for either alloy. It is known that different hydrogen concentration profiles are created depending on the charging method [16, 55]. Electrochemical charging creates a large concentration of diffusible hydrogen in sites like grain boundaries and interstitials, while high-temperature gaseous charging also fills up traps with a high trap energy while providing the hydrogen with enough energy to overcome shallow traps [14, 31]. The lowest activation energy measured in this research was 43 kJ/mol for misfit dislocations around small TiC precipitates, which is not considered diffusible hydrogen, nor irreversibly trapped hydrogen [52, 53]. Similarly, C-vacancies on the coherent VC interface fall in this category with an activation energy of around 60 kJ/mol. Since these activation energies do not fall into the reversible category (< 30 kJ/mol [56]), they are not expected to contribute to HE, which was

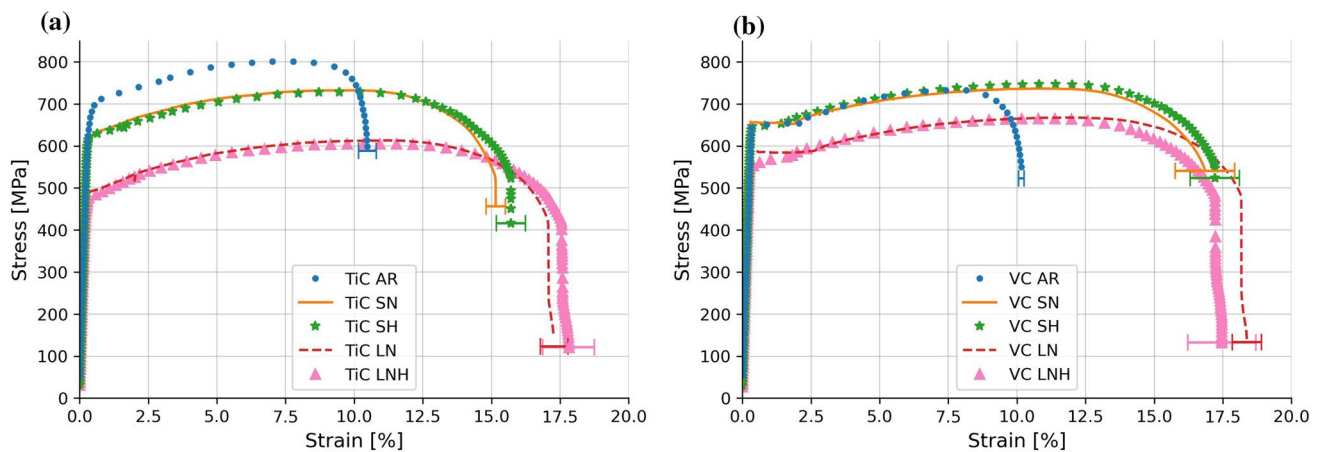


**Figure 10** Representative Slow Strain Rate Tensile (SSRT) curves for all conditions in **a** the TiC alloy and **b** the VC alloy. Error bars show standard deviations in the fracture strain [%].

also found in this study. Several specimens were subjected to a post-mortem TDS cycle after tensile testing to exclude the possibility that hydrogen effusion from the specimens during the test was the reason HE was not observed. These measurements showed no decrease in hydrogen content over the duration of the tensile test. These traps therefore contribute to preventing HE in the alloys even though they are not completely irreversible. Moreover, Depover et al. showed that these traps can be filled through electrochemical charging at room temperature [12], while they were also charged through high-temperature gaseous charging in this study. This means that they can act as hydrogen sinks in different service conditions. Optimisation of these types of hydrogen traps could lead to creating more hydrogen resistant steels.

This work is unique compared to similar works [14, 16] in the fact that high-temperature as well as low-temperature peaks were observed after high-temperature gaseous charging. This is most likely a result of performing both the heat treatment and the cooling down in hydrogen gas. During the cooling down, the available energy for hydrogen to overcome shallower traps gradually decreases, and hydrogen is expected to occupy these sites eventually. Depover et al. [12] showed that hydrogen traps belonging to misfit dislocations, the lowest energy traps found in this work, can also be charged through electrochemical methods. An effect of these traps on HE was observed in their study, whereas the material was not embrittled in this research. This suggests a more favourable hydrogen trap occupation after gaseous charging when compared to electrochemical charging that does not result in any HE.

## Conclusions

In this work, TiC and VC precipitate growth and hydrogen absorption as a result of high-temperature gaseous hydrogen charging were successfully characterised using TEM, EBSD and TDS. Moreover, direct observation of hydrogen trapping in incoherent precipitates was made using SIMS. By combining these techniques, the following conclusions could be drawn on the hydrogen trapping and embrittlement behaviour of titanium- and vanadium carbide-containing steels:

- High-temperature gaseous charging is shown to be a suitable way to charge steel containing deep hydrogen traps. The TiC- and VC-containing alloys

were charged with hydrogen up to 0.91 and 0.44 wppm, respectively.

- Little effect of TiC precipitate size on hydrogen trapping was found. All precipitates were either semi-coherent or incoherent even after a 2 h heat treatment duration. Coherent TiC precipitates trap hydrogen in misfit dislocations around the semi-coherent interface with an activation energy of 43 kJ/mol. Most hydrogen was trapped in carbon vacancies near the interface of larger incoherent particles, for which an activation energy was not obtained.
- An effect of VC precipitate size was observed in the form of a reduction in low-temperature hydrogen trapping after 20 h of heat treatment. The hydrogen traps after the 2 h heat treatment were characterised as mainly carbon vacancies on the coherent VC interface with an energy of between 53 and 72 kJ/mol. After the 20 h treatment, most hydrogen is stored in the bulk of large incoherent vanadium carbides with a large amount of carbon vacancies, for which no activation energy was found in this work.
- Direct observation of hydrogen trapping in incoherent TiC and VC carbides was made using SIMS. Large TiC precipitates were shown to vary in the degree of hydrogen absorption and to preferentially trap hydrogen near the precipitate interface. VC precipitates were shown to trap hydrogen throughout the bulk, but were present in smaller quantities, leading to an overall lower absorbed hydrogen content. More SIMS analysis is required to further elaborate on the trapping characteristics of incoherent precipitates.
- Neither of the heat treatment conditions resulted in any observable HE after mechanical characterisation. This proves that nano-carbides can successfully be used as a hydrogen sink as well as a strengthening mechanism in steels after high-temperature gaseous hydrogen charging. However, further study using electrochemical charging is recommended to compare the effects of different charging conditions on HE.

## Acknowledgements

The authors would like to thank TATA Steel in IJmuiden for providing the material for this research,



Dr. Ir. F. D. Tichelaar at the department of Quantum Nanoscience at TU Delft for the in-depth TEM analysis and Ing. Hans Brouwer from the department of Materials Science & Engineering for providing his furnaces and assistance.

### Author contributions

Conceptualisation was performed by all authors; investigation by TB, AK; writing—original draft by TB; writing—review & editing by all authors; supervision by SE, AB, VP; funding acquisition by SE, VP.

### Funding

This research was carried out under project number N19009 in the framework of the Partnership Program of the Materials innovation institute M2i ([www.m2i.nl](http://www.m2i.nl)) and the Netherlands Organization for Scientific Research ([www.nwo.nl](http://www.nwo.nl)). The SIMS part of the work was funded by the Luxembourg National Research Fund (FNR) through the grant PRIDE21/16758661/HYMAT. For the Titan TEM results, we acknowledge support from the Kavli Institute of Nanoscience, Delft University of Technology and the Netherlands Electron Microscopy Infrastructure (NEMI), project number 184.034.014, part of the National Roadmap and financed by the Dutch Research Council (NWO).

### Data availability

The research data can be made available upon request.

### Declarations

**Conflict of interest** The authors declare that they have no known competing financial interests that could have appeared to influence the work reported in this paper.

**Supplementary Information** The online version contains supplementary material available at <https://doi.org/10.1007/s10853-024-09611-7>.

**Open Access** This article is licensed under a Creative Commons Attribution 4.0 International License,

which permits use, sharing, adaptation, distribution and reproduction in any medium or format, as long as you give appropriate credit to the original author(s) and the source, provide a link to the Creative Commons licence, and indicate if changes were made. The images or other third party material in this article are included in the article's Creative Commons licence, unless indicated otherwise in a credit line to the material. If material is not included in the article's Creative Commons licence and your intended use is not permitted by statutory regulation or exceeds the permitted use, you will need to obtain permission directly from the copyright holder. To view a copy of this licence, visit <http://creativecommons.org/licenses/by/4.0/>.

### References

- [1] Galán J, Samek L, Verleysen P, Verbeken K, Houbaert Y (2012) Advanced high strength steels for automotive industry. *Rev Metal* 48(2):118–131
- [2] Serrenho AC, Norman JB, Allwood JM (2017) The impact of reducing car weight on global emissions: the future fleet in great Britain. *Philos Trans R Soc A Math Phys Eng Sci* 375(2095):20160364
- [3] Zhang W, Xu J (2022) Advanced lightweight materials for automobiles: a review. *Mater Design* 221:110994
- [4] Zhao J, Jiang Z (2018) Thermomechanical processing of advanced high strength steels. *Prog Mater Sci* 94:174–242
- [5] Lovicu G, Bottazzi M, D'aiuto F, De Sanctis M, Dimatteo A, Santus C, Valentini R (2012) Hydrogen embrittlement of automotive advanced high-strength steels. *Metall Mater Trans A Phys Metall Mater Sci* 43(11):4075–4087
- [6] Liu Q, Zhou Q, Venezuela J, Zhang M, Atrens A (2017) Hydrogen influence on some advanced high-strength steels. *Corros Sci* 125(March):114–138. <https://doi.org/10.1016/j.corsci.2017.06.012>
- [7] Dwivedi SK, Vishwakarma M (2019) Effect of hydrogen in advanced high strength steel materials. *Int J Hydrog Energy* 44(51):28007–28030. <https://doi.org/10.1016/j.ijhydene.2019.08.149>
- [8] Raabe D, Sun B, Kwiatkowski Da Silva A, Gault B, Yen HW, Sedighiani K, Thoudden Sukumar P, Souza Filho IR, Katnagallu S, Jäggle E, Kürnstener P, Kusampudi N, Stephenson L, Herbig M, Liebscher CH, Springer H, Zaefferer S, Shah V, Wong SL, Baron C, Diehl M, Roters F, Ponge D (2020) Current challenges and opportunities in microstructure-related properties of advanced high-strength steels.

- Metall Mater Trans A Phys Metall Mater Sci 51(11):5517–5586. <https://doi.org/10.1007/s11661-020-05947-2>
- [9] Drexler A, Helic B, Silvayeh Z, Mraczek K, Sommitsch C, Domitner J (2022) The role of hydrogen diffusion, trapping and desorption in dual phase steels. *J Mater Sci* 57(7):4789–4805. <https://doi.org/10.1007/s10853-021-06830-0>
- [10] Nagao A, Martin ML, Dadfarnia M, Sofronis P, Robertson IM (2014) The effect of nanosized (Ti, Mo)C precipitates on hydrogen embrittlement of tempered lath martensitic steel. *Acta Mater* 74:244–254
- [11] Laureys A, Claeys L, De Seranno T, Depover T, Van den Eeckhout E, Petrov R, Verbeken K (2018) The role of titanium and vanadium based precipitates on hydrogen induced degradation of ferritic materials. *Mater Charact* 144(May):22–34. <https://doi.org/10.1016/j.matchar.2018.06.030>
- [12] Depover T, Verbeken K (2016) Evaluation of the effect of v4c3 precipitates on the hydrogen induced mechanical degradation in fe-cv alloys. *Mater Sci Eng A* 675:299–313
- [13] Depover T, Verbeken K (2018) The detrimental effect of hydrogen at dislocations on the hydrogen embrittlement susceptibility of Fe-C-X alloys: An experimental proof of the HELP mechanism. *Int J Hydrog Energy* 43(5):3050–3061. <https://doi.org/10.1016/j.ijhydene.2017.12.109>
- [14] Vandewalle L, Depover T, Verbeken K (2023) Hydrogen trapping of carbides during high temperature gaseous hydrogenation. *Int J Hydrog Energy* 48(82):32158–32168. <https://doi.org/10.1016/j.ijhydene.2023.04.348>
- [15] Malard B, Remy B, Scott C, Deschamps A, Chêne J, Dieudonné T, Mathon MH (2012) Hydrogen trapping by VC precipitates and structural defects in a high strength Fe–Mn–C steel studied by small-angle neutron scattering. *Mater Sci Eng A* 536:110–116. <https://doi.org/10.1016/j.msea.2011.12.080>
- [16] Pérez Escobar D, Wallaert E, Duprez L, Atrens A, Verbeken K (2013) Thermal desorption spectroscopy study of the interaction of hydrogen with TiC precipitates. *Metals Mater Int* 19(4):741–748. <https://doi.org/10.1007/s12540-013-4013-7>
- [17] Wei FG, Tsuzaki K (2006) Quantitative analysis on hydrogen trapping of TiC particles in steel. *Metall Mater Trans A Phys Metall Mater Sci* 37(2):331–353. <https://doi.org/10.1007/s11661-006-0004-3>
- [18] Wei FG, Hara T, Tsuchida T, Tsuzaki K (2003) Hydrogen trapping in quenched and tempered 0.42 c-0.30 ti steel containing bimodally dispersed TiC particles. *ISIJ Int* 43(4):539–547
- [19] Turnbull A (2012) Gaseous hydrogen embrittlement of materials in energy technologies. Elsevier, pp 89–128
- [20] Wang M, Akiyama E, Tsuzaki K (2007) Effect of hydrogen on the fracture behavior of high strength steel during slow strain rate test. *Corros Sci* 49(11):4081–4097. <https://doi.org/10.1016/j.corsci.2007.03.038>
- [21] Barrera O, Bombac D, Chen Y, Daff TD, Galindo-Nava E, Gong P, Haley D, Horton R, Katzarov I, Kermodé JR, Liverani C, Stopher M, Sweeney F (2018) Understanding and mitigating hydrogen embrittlement of steels: a review of experimental, modelling and design progress from atomistic to continuum. *J Mater Sci* 53(9):6251–6290. <https://doi.org/10.1007/s10853-017-1978-5>
- [22] Koyama M, Tasan CC, Akiyama E, Tsuzaki K, Raabe D (2014) Hydrogen-assisted decohesion and localized plasticity in dual-phase steel. *Acta Mater* 70:174–187. <https://doi.org/10.1016/j.actamat.2014.01.048>
- [23] Ronevich JA, Somerday BP (2016) Assessing gaseous hydrogen assisted fatigue crack growth susceptibility of pipeline steel weld fusion zones and heat affected zones. *Mater Perform Charact* 5(3):290–304. <https://doi.org/10.1520/MPC20150057>
- [24] Depover T, Verbeken K (2016) The effect of TiC on the hydrogen induced ductility loss and trapping behavior of Fe–C–Ti alloys. *Corros Sci* 112:308–326. <https://doi.org/10.1016/j.corsci.2016.07.013>
- [25] Wei F, Hara T, Tsuzaki K (2004) Precise determination of the activation energy for desorption of hydrogen in two Ti-added steels by a single thermal-desorption spectrum. *Metall Mater Trans* 35(3):587–597
- [26] Wei FG, Tsuzaki K (2004) Hydrogen absorption of incoherent TiC particles in iron from environment at high temperatures. *Metall Mater Trans A Phys Metall Mater Sci* 35A(10):3155–3163. <https://doi.org/10.1007/s11661-004-0060-5>
- [27] Di Stefano D, Nazarov R, Hickel T, Neugebauer J, Mrovec M, Elsässer C (2016) First-principles investigation of hydrogen interaction with tic precipitates in  $\alpha$ -fe. *Phys Rev B* 93(18):184108
- [28] Takahashi J, Kawakami K, Kobayashi Y, Tarui T (2010) The first direct observation of hydrogen trapping sites in TiC precipitation-hardening steel through atom probe tomography. *Scr Mater* 63(3):261–264. <https://doi.org/10.1016/j.scriptamat.2010.03.012>
- [29] Sagar S, Sluiter MH, Dey P (2024) First—principles study of hydrogen—carbide interaction in bcc Fe. *Int J Hydrog Energy* 50:211–223. <https://doi.org/10.1016/j.ijhydene.2023.09.222>
- [30] Salehin R, Thompson GB, Weinberger CR (2022) Hydrogen trapping and storage in the group IVB–VIB transition metal carbides. *Mater Design* 214:110399. <https://doi.org/10.1016/j.matdes.2022.110399>

- [31] Takahashi J, Kawakami K, Kobayashi Y (2018) Origin of hydrogen trapping site in vanadium carbide precipitation strengthening steel. *Acta Mater* 153:193–204
- [32] Restrepo SE, Di Stefano D, Mrovec M, Paxton AT (2020) Density functional theory calculations of iron-vanadium carbide interfaces and the effect of hydrogen. *Int J Hydrog Energy* 45(3):2382–2389
- [33] Zhang B, Su J, Wang M, Liu Z, Yang Z, Militzer M, Chen H (2021) Atomistic insight into hydrogen trapping at MC/BCC-Fe phase boundaries: the role of local atomic environment. *Acta Mater* 208:116744
- [34] Baker R (1959) Precipitation processes in steels. *ISI Spec Rep* 64:1
- [35] Takahashi J, Kawakami K, Tarui T (2012) Direct observation of hydrogen-trapping sites in vanadium carbide precipitation steel by atom probe tomography. *Scr Mater* 67(2):213–216
- [36] Kawakami K, Matsumiya T (2012) Numerical analysis of hydrogen trap state by tic and v4c3 in BCC-Fe. *ISIJ Int* 52(9):1693–1697
- [37] Ma Y, Shi Y, Wang H, Mi Z, Liu Z, Gao L, Yan Y, Su Y, Qiao L (2020) A first-principles study on the hydrogen trap characteristics of coherent nano-precipitates in  $\alpha$ -Fe. *Int J Hydrog Energy* 45(51):27941–27949. <https://doi.org/10.1016/j.ijhydene.2020.07.123>
- [38] Tang S, Li L, Yan H, Jin J, Peng Q, Cai M, Li J, Liu Z, Wang G (2023) Hydrogen trapping in vanadium carbide alloyed with transition metals. *Nuclear Mater Energy* 36(September):101504. <https://doi.org/10.1016/j.nme.2023.101504>
- [39] Wei FG, Hara T, Tsuzaki K (2004) High-resolution transmission electron microscopy study of crystallography and morphology of TiC precipitates in tempered steel. *Philos Mag* 84(17):1735–1751. <https://doi.org/10.1080/14786430310001638762>
- [40] Pressouyre G, Bernstein I (1978) A quantitative analysis of hydrogen trapping. *Metall Trans A* 9:1571–1580
- [41] Tang S, Li LX, Peng Q, Yan HL, Cai MH, Li JP, Liu ZY, Wang GD (2022) First-principles insights into hydrogen trapping in interstitial-vacancy complexes in vanadium carbide. *Phys Chem Chem Phys* 24(34):20400–20408. <https://doi.org/10.1039/d2cp02425j>
- [42] Seo HJ, Kim JN, Jo JW, Lee CS (2021) Effect of tempering duration on hydrogen embrittlement of vanadium-added tempered martensitic steel. *Int J Hydrog Energy* 46(37):19670–19681. <https://doi.org/10.1016/j.ijhydene.2021.03.109>
- [43] Sun X, Kang J, Yong Q (2020) Revealing the difference of precipitation kinetics between TiC and VC in low-carbon tempered martensitic steels. *J Mater Sci* 55(33):16018–16032. <https://doi.org/10.1007/s10853-020-05176-3>
- [44] T.C. software AB. Thermo-Calc version 2021 (2021)
- [45] Ioannidou C, Arechabaleta Z, Navarro-López A, Rijkensberg A, Dalgliesh RM, Kölling S, Bliznuk V, Pappas C, Sietsma J, van Well AA, Offerman SE (2019) Interaction of precipitation with austenite-to-ferrite phase transformation in vanadium micro-alloyed steels. *Acta Mater* 181:10–24. <https://doi.org/10.1016/j.actamat.2019.09.046>
- [46] De Castro O, Audinot JN, Hoang HQ, Coulbary C, Bouton O, Barraha R, Ost A, Stoffels C, Jiao C, Dutka M et al (2022) Magnetic sector secondary ion mass spectrometry on fib-sem instruments for nanoscale chemical imaging. *Analyt Chem* 94(30):10754–10763
- [47] Andersen D, Chen H, Pal S, Cressa L, De Castro O, Wirtz T, Schmitz G, Eswara S (2023) Correlative high-resolution imaging of hydrogen in mg2ni hydrogen storage thin films. *Int J Hydrog Energy* 48(37):13943–13954
- [48] Kissinger HE (1957) Reaction kinetics in differential thermal analysis. *Analyt Chem* 29(11):1702–1706. <https://doi.org/10.1021/ac60131a045>
- [49] ASTM G142, Standard test method for determination of susceptibility of metals to embrittlement in hydrogen containing environments at high pressure, high temperature, or both. *ASTM Book of Standards 03(Reapproved 2016)* 1–8 (1998). <https://doi.org/10.1520/G0142-98R16.2>
- [50] ASTM G129, Standard practice for slow strain rate testing to evaluate the susceptibility of metallic materials to environmentally assisted cracking 1. *ASTM Book of Standards 00(Reapproved 2013)* 1–7 (2006). <https://doi.org/10.1520/G0129-00R06.2>
- [51] ASTM E1181-02, Standard test methods for characterizing duplex grain sizes. *ASTM Book of Standards 02(Reapproved 2008)* 1–15 (2008). <https://doi.org/10.1520/E1181-02R23.Copyright>
- [52] Drexler A, Vandewalle L, Depover T, Verbeken K, Domitner J (2021) Critical verification of the Kissinger theory to evaluate thermal desorption spectra. *Int J Hydrog Energy* 46(79):39590–39606. <https://doi.org/10.1016/j.ijhydene.2021.09.171>
- [53] Castaño Rivera P, Ramunni VP, Bruzzoni P (2012) Hydrogen trapping in an API 5L X60 steel. *Corros Sci* 54(1):106–118. <https://doi.org/10.1016/j.corsci.2011.09.008>
- [54] Wei FG, Hara T, Tsuchida T, Tsuzaki K (2003) Hydrogen trapping in quenched and tempered 0.42C–0.30Ti steel containing bimodally dispersed TiC particles. *ISIJ Int* 43(4):539–547. <https://doi.org/10.2355/isijinternational.43.539>
- [55] Zhao Y, Seok MY, Choi IC, Lee YH, Park SJ, Ramamurthy U, Suh JY, Jang JI (2015) The role of hydrogen in

hardening/softening steel: influence of the charging process. *Scr Mater* 107:46–49. <https://doi.org/10.1016/j.scripamat.2015.05.017>

[56] Dadfarnia M, Sofronis P, Neeraj T (2011) Hydrogen interaction with multiple traps: Can it be used to mitigate embrittlement? *Int J Hydrog Energy* 36(16):10141–10148

**Publisher's Note** Springer Nature remains neutral with regard to jurisdictional claims in published maps and institutional affiliations.